

Differentiable Particle-Mesh Ewald with Cartesian Tensor Message Passing for Learning Long-Range Electrostatics and Dipole Response

Zhiyue Guo¹, Junjie Wang^{1*}, Haoting Zhang¹, Zhixin Liang¹
Ziyang Yang¹, Yujian Pan¹, Jian Sun^{1*}

¹National Laboratory of Solid State Microstructures,
School of Physics and Collaborative Innovation Center
of Advanced Microstructures,
Nanjing University, Nanjing 210093, China

Abstract

Machine learning interatomic potentials (MLIPs) can approach quantum accuracy for short-range chemistry, yet most architectures remain fundamentally local and fail to describe the long-range electrostatic and polarization interactions essential for ionic, polar, and interfacial systems. Recent and contemporaneous Ewald-based MLIPs have shown that locally predicted electrostatic variables can recover important long-range physics, including multipolar response. However, many energy-based implementations still evaluate the reciprocal term by direct sums over k vectors. This leaves a practical gap between long-range MLIP development and production molecular dynamics, where particle-mesh Ewald (PME) with $O(N \log N)$ scaling is the standard. Here we introduce a fully differentiable PME framework for learned charges and, centrally, learned atomic dipoles within an $E(n)$ -equivariant Cartesian tensor message passing network. Charges are predicted from scalar local features, while dipole vectors are predicted from equivariant vector features and enter the same particle-mesh solver as an effective bound charge density. This dipolar density is constructed by analytic real-space gradients of the Hockney–Eastwood spline assignment weights, allowing charge–dipole and dipole–dipole

long-range forces to be trained end-to-end through FFT-space electrostatics without direct charge or dipole supervision. On a charged-dimer test case, the differentiable PME module reproduces explicit Ewald energies and forces to numerical precision when the assignment-kernel deconvolution is enabled. On molten NaCl, the charge+dipole long-range channel gives the lowest force RMSE among the tested models while all energy RMSE values remain in the sub-meV/atom regime. Timing tests show the expected crossover from explicit Ewald summation to particle-mesh scaling. These results identify differentiable dipole PME as a scalable route toward polarization-aware MLIPs for condensed-phase and interfacial systems.

1 Introduction

Machine learning interatomic potentials (MLIPs) have transformed atomistic materials modeling over the past decade, achieving first-principles accuracy at a fraction of the computational cost [1, 2, 3, 4, 5, 6, 7, 9, 10, 12, 13]. By learning the Born–Oppenheimer potential energy surface directly from electronic structure reference data, these methods have enabled simulations at time and length scales far beyond the reach of *ab initio* molecular dynamics.

This progress has followed a clear architectural trajectory. Early neural-network and kernel potentials demonstrated that atom-centered descriptors could learn accurate local energy decompositions [1, 2, 5], while moment and spectral descriptor families made this idea systematically improvable for materials [3, 4]. Deep message-passing and equivariant architectures then replaced fixed descriptors with learned geometric representations. These models respect the fundamental symmetries of atomistic systems: the total energy is invariant to global translations and permutations of equivalent atoms, atom-wise features are permutation equivariant with respect to atom indexing, and scalar, vector, and tensor channels transform consistently under rotations. This symmetry-aware structure improves data efficiency for energies, forces, and tensorial properties [7, 8, 9, 10, 11, 12].

Despite these advances, most MLIPs still rely on a *locality ansatz*: the total energy is decomposed into atom-centered contributions that depend only on the atomic environment within a finite cutoff radius r_c . The assumption is physically motivated by the nearsightedness of electronic matter and gives the linear scaling that makes large-scale simulations possible. It is also the source of a sharp limitation. Coulomb interactions decay as r^{-1} , charge–dipole interactions as r^{-2} , and polarization response can depend on the dielectric environment over length scales far beyond a typical 4–6 Å local cutoff. Short-range MLIPs can therefore interpolate accurately within many

covalent and metallic training domains while still failing in ionic materials, polar molecular liquids, solid electrolytes [14], solid–liquid interfaces, and any system where charge redistribution or long-range screening controls the forces [15, 16].

Existing long-range MLIP strategies can be organized by how they relax this locality constraint. The most direct route is to enlarge the receptive field, either by increasing the cutoff, stacking more message-passing layers, or using multiscale short/long-cutoff modules. This keeps the model architecture close to standard local MLIPs, but the cost and the number of neighbors grow rapidly, while distant electrostatic information is still only represented implicitly. A second route adds physically motivated energy terms. PhysNet and SpookyNet, for example, combine neural short-range energies with learned charges, dispersion corrections, total-charge or spin information, and damped electrostatic terms [24, 25]. Such decompositions impose useful asymptotic structure, but the learned electrostatic variables may depend on a chosen charge convention and are not always sufficient to describe non-local charge redistribution.

Global electrostatic-variable models address part of this problem by constraining the charges themselves. Charge-equilibration approaches predict local electronegativities and hardnesses and then solve a global minimization problem to obtain charges [17, 18, 19, 20, 21]. These methods can capture non-local charge transfer, but they introduce an additional global solve and inherit the well-known ambiguities of partial-charge definitions. Deep potential long-range (DPLR) models avoid direct atomic-charge fitting by using maximally localized Wannier centers as physically motivated charge carriers [26]; this provides a smoother description of electrostatics but requires Wannier information in the reference data. Classical polarizable force fields offer a complementary lesson: induced dipoles and atomic multipoles are often essential for dielectric response beyond fixed charges [22, 23], but in conventional force fields these variables are usually parameterized rather than learned end-to-end from quantum-mechanical energy-force data.

A third family uses global descriptors, reciprocal operators, or non-local message passing to carry information beyond the local cutoff. Reciprocal-space neural networks construct structure-factor-like descriptors or learned reciprocal potentials from the full simulation cell, allowing local MLIPs to access full-cell information without assigning explicit atomic charges [27]. LODE-type descriptors augment local representations with fields generated by long-ranged density kernels [28, 29]. Ewald message passing instead uses reciprocal-space filters as a non-local message-passing operation [30]. Along the same line, LOREM treats inverse-power-law potential evaluation as equivariant message passing: scalar and higher-order equivariant charge

channels transmit orientation-dependent geometric information beyond the cutoff [31]. These latent channels are not identical to physical atomic multipoles, but they are closely related in spirit to using high-order tensor representations as carriers of long-range information.

A complementary energy-based route is to predict electrostatic variables and evaluate a separate long-range energy. The Latent Ewald Summation (LES) framework uses local descriptors to predict latent scalar charges and trains them only through total energies and forces [32, 34], avoiding direct supervision on convention-dependent partial charges. Kim et al. [33] recently extended this strategy to a polarizable multipole hierarchy, including monopoles, dipoles, quadrupoles, and non-self-consistent linear response. Together, these developments show a broad movement toward combining local equivariant representations with global electrostatic or reciprocal-space operators. They differ in what is made non-local—descriptors, messages, latent charges, or multipoles—and should therefore be viewed as complementary rather than as a single settled formulation.

The specific gap addressed here is the numerical realization of an energy-based learned charge–dipole branch for periodic, large-scale force-field training. A direct Ewald implementation evaluates the reciprocal-space contribution as a sum over all integer vectors \mathbf{n} within a cutoff sphere in k -space [37]. For a system of N atoms, the number of reciprocal-space vectors grows super-linearly, yielding an effective complexity of $O(N^{3/2})$ or $O(N^2)$ depending on the choice of Ewald splitting parameter [38]. This is accurate and useful for reference calculations, but it contrasts with the state of practice in classical molecular dynamics: major production MD codes—AMBER, GROMACS, LAMMPS, NAMD, CHARMM—evaluate long-range electrostatics using the particle-mesh Ewald (PME) method [39, 40, 41, 42, 43, 44, 45], which accelerates reciprocal-space evaluation to $O(N \log N)$ through the use of the fast Fourier transform (FFT) on a regular mesh. For atomistic ML, Loche et al. recently exposed the torch-pme library [46]. The charge-only PME branch used here was developed with reference to this framework, while the formulation introduced below additionally handles learned dipolar densities in a unified differentiable mesh pipeline. For learned electrostatic energy models that rely on direct reciprocal-vector sums, replacing the sum by a differentiable particle-mesh operation is therefore an important step toward deployable large-scale simulations.

In this work, we bridge this gap by introducing a fully differentiable particle-mesh Ewald framework integrated with an $E(n)$ -equivariant Cartesian tensor message passing architecture [12]. The long-range solver is implemented as a native PyTorch module, so gradients propagate end-to-end from the electrostatic energy through mesh assignment, FFT-based reciprocal-

space evaluation, and back to the latent charge and dipole readouts while retaining the $O(N \log N)$ scaling of PME.

We examine the framework on two completed example systems. The first is a charged-dimer test case based on the charged molecular dimer data discussed by King et al. [34], where long-range electrostatics dominate the interaction and PME can be compared directly against an explicit Ewald reference. The second uses liquid NaCl structures from the density-based long-range descriptor study of Faller et al. [36], which was also used as a molten-salt example in the LES work [32]. Replicated NaCl supercells are used strictly for timing. These examples establish the two claims supported by the present data: long-range charge/dipole channels improve the learned force field in systems with strong electrostatics, and the differentiable PME implementation recovers Ewald-level reciprocal-space accuracy at particle-mesh cost. The total energy decomposes as $E_{\text{total}} = \sum_i E_i^{\text{sr}} + E^{\text{lr}}(\{q_i\}, \{\boldsymbol{\mu}_i\})$, where the short-range term is predicted by the equivariant message-passing network and the long-range term is evaluated through the differentiable PME pipeline with its gradient flowing end-to-end back to the network parameters. In this formulation, PME is not only an efficient electrostatic solver but also a trainable long-range layer that allows charge-dipole physics to be learned together with the short-range potential.

2 Theory and Methodology

The overall HotPP-LR architecture is summarized in Fig. 1. Atomic structures are first encoded by the short-range HotPP Cartesian tensor message-passing backbone. Separate readout heads then produce local site energies, latent atomic charges, and latent atomic dipoles. The site energies define the short-range contribution, whereas the learned charges and dipoles are deposited onto the PME mesh to evaluate the non-local electrostatic contribution. The total energy remains differentiable with respect to positions and network parameters, so force training can update both the short-range backbone and the long-range electrostatic readouts.

2.1 Cartesian tensor message passing

We adopt the $E(n)$ -equivariant Cartesian tensor message passing framework introduced in Ref. 12 as the short-range backbone of our model. Because the architecture and its tensor algebra are described in detail in the original HotPP paper, we only summarize the ingredients needed to define the long-range extension.

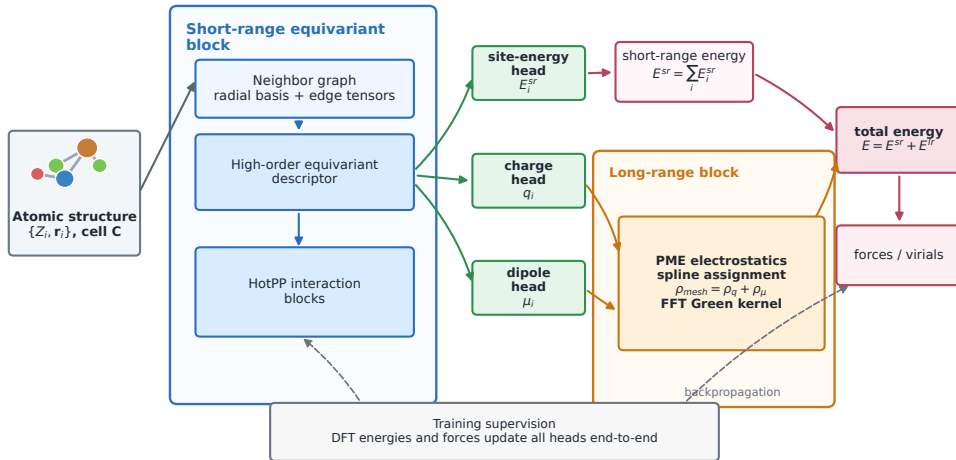


Figure 1: Schematic architecture of the HotPP-LR model. The short-range branch is the $E(n)$ -equivariant HotPP Cartesian tensor message-passing network. Scalar and vector features feed separate site-energy, charge, and dipole readouts. The site-energy head gives E^{sr} , while the charge and dipole heads feed a differentiable PME branch that constructs ρ_{mesh} , applies the FFT-space Green kernel, and returns E^{lr} . The sum $E^{\text{sr}} + E^{\text{lr}}$ is differentiated end-to-end to obtain forces and train all readout heads from energy-force data.

For each atom, HotPP stores local features as Cartesian tensors of different ranks. The scalar rank, denoted here as $\mathbf{h}_i^{(t,0)}$, carries rotation-invariant chemical information; the vector rank $\mathbf{h}_i^{(t,1)}$ carries directional information; and higher-rank tensor features can encode more complex angular response. Message-passing layers update these features by combining radial basis functions with geometric edge tensors, followed by self-interaction, nonlinear activation, and residual mixing. This gives an $E(n)$ -equivariant local representation after T layers while avoiding spherical-harmonic basis transformations.

In the present work, we keep this HotPP backbone unchanged and use it to provide the local, short-range part of the potential. Our contribution begins at the readout level: the same final local features that predict the short-range site energy are also used to predict latent charges and dipoles, which are then passed to a differentiable PME solver.

2.2 Predicting charges and dipoles from local features

A key advantage of this Cartesian tensor representation is that different physical observables naturally emerge from different ranks of the node features. We attach a multi-head readout layer after the final message-passing layer to predict:

- **Atomic partial charges** q_i from the scalar ($L = 0$) features:

$$q_i = \text{MLP}_q(\mathbf{h}_i^{(T,0)}), \quad (1)$$

where MLP_q is a two-layer perceptron with SiLU activation.

- **Atomic dipole vectors** $\boldsymbol{\mu}_i$ from the vector ($L = 1$) features:

$$\boldsymbol{\mu}_i = \text{MLP}_\mu(\mathbf{h}_i^{(T,1)}), \quad (2)$$

where MLP_μ acts on the channel dimension, preserving the Cartesian vector index. The output is a 3-dimensional vector $\boldsymbol{\mu}_i = (\mu_i^x, \mu_i^y, \mu_i^z)$ that transforms covariantly under rotations.

- **Short-range site energy** E_i^{sr} from the scalar features:

$$E_i^{\text{sr}} = \text{MLP}_E(\mathbf{h}_i^{(T,0)}). \quad (3)$$

Crucially, the charges q_i and dipoles $\boldsymbol{\mu}_i$ are trained *without direct supervision*. No reference charges, dipole moments, or electrostatic potentials are provided during training—only total energies and atomic forces. The learning signal for these electrostatically meaningful quantities flows entirely through the long-range energy term (Section 2.3) and the total force $\mathbf{F}_i = -\partial E_{\text{total}}/\partial \mathbf{r}_i$, which couples the spatial derivatives of E^{lr} back to the predicted charges and dipoles via automatic differentiation. After training, the learned charges and dipole-like vectors provide a decomposition of the electrostatic response. For finite non-periodic structures, a molecular dipole can be constructed from both charge positions and local dipoles, $\mathbf{M} = \sum_i q_i \mathbf{r}_i + \sum_i \boldsymbol{\mu}_i$ after applying the fixed sign convention of the dipole readout. For periodic condensed phases, the corresponding polarization must be interpreted with the usual periodic-boundary conventions rather than as a unique absolute dipole moment.

2.3 Differentiable Particle-Mesh Ewald

We now present the central methodological contribution of this work: a fully differentiable particle-mesh Ewald (PME) module that computes an FFT-accelerated screened reciprocal-space electrostatic term from predicted atomic multipoles at $O(N \log N)$ cost and supports end-to-end gradient back-propagation. By “fully differentiable” we mean that the entire computational graph—from the MPNN-predicted charges and dipoles through discrete mesh assignment (indexed scatter), forward and inverse real-to-complex FFTs, k -space Green’s function multiplication, influence function correction, and energy summation—is constructed from native PyTorch operations whose analytical gradients compose correctly under `autograd`, enabling stable training without surrogate loss functions or gradient approximations. Unlike a standalone classical Ewald calculation, the neural-potential module does not evaluate an explicit real-space $\text{erfc}(ar)/r$ pair term. The mesh term represents the smooth long-range channel, while the complementary short-range part is learned by the local HotPP energy. For comparison and validation, our implementation also provides a conventional Ewald summation baseline [37], which we use to assess PME accuracy in Section 3.

2.3.1 Mesh construction

Given a periodic simulation cell defined by the 3×3 matrix \mathbf{C} whose rows are the lattice vectors, the inverse cell is \mathbf{C}^{-1} . We denote the three direct lattice vectors by $\mathbf{a}_x, \mathbf{a}_y, \mathbf{a}_z$, i.e., the rows of \mathbf{C} . The corresponding reciprocal basis vectors $\mathbf{b}_x, \mathbf{b}_y, \mathbf{b}_z$ are the rows of $2\pi\mathbf{C}^{-T}$, so that $\mathbf{a}_\alpha \cdot \mathbf{b}_\beta = 2\pi\delta_{\alpha\beta}$. The mesh dimensions N_x, N_y, N_z are determined from a target grid spacing Δ :

$$N_\alpha^{\text{target}} = \left\lceil \frac{2\|\mathbf{a}_\alpha\|}{\Delta} + 1 \right\rceil, \quad \alpha \in \{x, y, z\}, \quad (4)$$

where \mathbf{a}_α denotes the α -th row of \mathbf{C} . We provide three strategies for mapping the target dimensions to the actual mesh size, each offering a different tradeoff between FFT efficiency and monotonic convergence with respect to the grid spacing Δ :

- **Power-of-two:** $N_\alpha = 2^{\lceil \log_2(N_\alpha^{\text{target}}) \rceil}$. Fastest FFT, but the energy is a step function of Δ —small reductions in Δ may not change N_α at all, complicating convergence studies.
- **Smooth (default):** N_α is the smallest integer $\geq N_\alpha^{\text{target}}$ whose prime factors belong to $\{2, 3, 5\}$. These numbers are nearly as FFT-friendly as powers of two while providing finer granularity and near-monotonic energy convergence.

- **Direct ceil:** $N_\alpha = \lceil N_\alpha^{\text{target}} \rceil$. Fully monotonic in Δ ; FFT performance may degrade for unfavorable N_α with large prime factors.

The grid spacing Δ and mesh strategy are user-specified hyperparameters; alternatively, the user may specify $[N_x, N_y, N_z]$ explicitly.

2.3.2 Hockney–Eastwood spline assignment

We distribute point charges and dipoles onto the regular mesh using the Hockney–Eastwood spline charge-assignment functions [49] summarized by Deserno and Holm [47, 48]. For an assignment order p (supporting $p = 1$ through $p = 7$), the one-dimensional weight function $W^{(p)}(\xi)$ is a compact piecewise polynomial of degree $p - 1$. These are the spline particle-mesh assignment weights, not the Lagrange interpolation weights used with the unmodified continuum Green function in the original PME construction.

Given an atomic position \mathbf{r}_i represented as a row vector, we first compute the fractional coordinates relative to the mesh: $\mathbf{s}_i = \mathbf{r}_i \mathbf{C}^{-1}$, then $\mathbf{x}_i = (N_x s_i^x, N_y s_i^y, N_z s_i^z)$. For odd assignment order p , the nearest mesh point is at $\mathbf{n}_i = \text{round}(\mathbf{x}_i)$, and the offset is $\boldsymbol{\xi}_i = \mathbf{x}_i - \mathbf{n}_i$. For even p , we use $\mathbf{n}_i = \lfloor \mathbf{x}_i \rfloor$ with offset $\boldsymbol{\xi}_i = \mathbf{x}_i - (\mathbf{n}_i + \frac{1}{2})$. The three-dimensional assignment weight is the separable product:

$$W_{ijk}(\mathbf{r}) = W^{(p)}(\xi^x - u_i) W^{(p)}(\xi^y - u_j) W^{(p)}(\xi^z - u_k), \quad (5)$$

where (u_i, u_j, u_k) enumerates the p^3 mesh points in the interpolation stencil centered at \mathbf{n}_i .

For predicted charges and dipoles, the mesh stores a single effective charge density. With the shorthand $W_x = W^{(p)}(\xi_i^x - u)$, $W_y = W^{(p)}(\xi_i^y - v)$, $W_z = W^{(p)}(\xi_i^z - w)$, and similarly $W'_x = \partial W^{(p)}(\xi_i^x - u) / \partial \xi_i^x$, the value scattered from atom i to the stencil point $(n_i^x + u, n_i^y + v, n_i^z + w)$ is

$$\begin{aligned} \rho_{\text{mesh}}(\mathbf{n}) = \sum_{i=1}^N \sum_{(u,v,w)} \delta_{\mathbf{n}, \mathbf{n}_i + (u,v,w)}^{\text{P}} & \left[q_i W_x W_y W_z \right. \\ & + N_x (\boldsymbol{\mu}_i \cdot \mathbf{C}_{:x}^{-1}) W'_x W_y W_z \\ & + N_y (\boldsymbol{\mu}_i \cdot \mathbf{C}_{:y}^{-1}) W_x W'_y W_z \\ & \left. + N_z (\boldsymbol{\mu}_i \cdot \mathbf{C}_{:z}^{-1}) W_x W_y W'_z \right], \quad (6) \end{aligned}$$

where the inner sum runs over the p stencil points along each dimension and δ^{P} is a periodic Kronecker delta on the mesh. Equivalently, if a stencil point falls outside the mesh, its three indices are wrapped back into the ranges

$0, \dots, N_x - 1, 0, \dots, N_y - 1$, and $0, \dots, N_z - 1$, respectively. Here $\mathbf{C}_{:\alpha}^{-1}$ denotes the α -th column of the inverse cell matrix. The first line is the monopole assignment; the remaining three lines are the dipolar effective charge density obtained by differentiating the same separable assignment kernel along the three mesh directions.

2.3.3 Influence function deconvolution

A subtle but consequential artifact of particle-mesh assignment is that the mesh density is a smoothed version of the particle density. A point charge is not placed on a single grid point; it is distributed over the nearby stencil by the assignment weights $W^{(p)}$. In continuum language, this operation is a convolution of the true particle density with the assignment kernel. Therefore, before considering the additional aliasing errors introduced by sampling on a finite grid, the leading reciprocal-space effect is simply a multiplication by the Fourier transform of the assignment kernel:

$$\tilde{\rho}_{\text{mesh}}(\mathbf{k}) = \tilde{\rho}_{\text{true}}(\mathbf{k}) \cdot \tilde{W}(\mathbf{k}), \quad (7)$$

where $\tilde{W}(\mathbf{k})$ is the Fourier transform of the assignment function. For the separable assignment kernel used in our implementation, the frequency response is approximated in grid-index space as

$$B(\mathbf{n}) = \text{sinc}^p\left(\frac{n_x}{N_x}\right) \text{sinc}^p\left(\frac{n_y}{N_y}\right) \text{sinc}^p\left(\frac{n_z}{N_z}\right), \quad (8)$$

where $\mathbf{n} = (n_x, n_y, n_z)$ are the discrete FFT frequency indices and $\text{sinc}(x) = \sin(\pi x)/(\pi x)$ with $\text{sinc}(0) = 1$. This separable form is the standard sinc response associated with spline particle-mesh assignment [45]. Our implementation uses the separable factor in Eq. 8 as a lightweight deconvolution correction for the leading mesh assignment error.

This filtering modifies the high-frequency part of the reciprocal-space density and produces systematic mesh-dependent errors. At this detailed level, the correction is a simplified, P3M-inspired influence-correction strategy motivated by particle-mesh methods [49, 47, 48]: we reduce the leading assignment error by applying a deconvolution factor $\mathcal{C}(\mathbf{n})$ to the Green's function in reciprocal space:

$$\tilde{G}_{\text{corrected}}(\mathbf{k}) = \tilde{G}(\mathbf{k}) \cdot \mathcal{C}(\mathbf{n}), \quad \mathcal{C}(\mathbf{n}) = \frac{1}{|B(\mathbf{n})|^{2\gamma}}, \quad (9)$$

where γ is the implementation parameter `influence_power`. The default is $\gamma = 1$, so the correction is $1/|B|^2$. We do not use the full optimal P3M

influence function of Hockney–Eastwood or Deserno–Holm, which contains aliasing sums and depends on the chosen differentiation operator. Thus, the present method should not be described as a full optimal P3M implementation; it is a differentiable PME solver that borrows the P3M idea of assignment-kernel compensation through a simple separable deconvolution factor matched to the spline assignment response.

2.3.4 Reciprocal-space energy

The mesh density $\rho_{\text{mesh}}(n_x, n_y, n_z)$ is transformed to reciprocal space via a 3D real-to-complex FFT:

$$\tilde{\rho}(k_x, k_y, k_z) = \text{FFT}[\rho_{\text{mesh}}], \quad (10)$$

where the discrete FFT frequency indices \mathbf{n} are mapped to physical reciprocal vectors by $\mathbf{k} = n_x \mathbf{b}_x + n_y \mathbf{b}_y + n_z \mathbf{b}_z$ using the reciprocal basis vectors defined above.

The reciprocal-space Green’s function for the Gaussian-screened Coulomb interaction is:

$$\tilde{G}(\mathbf{k}) = \begin{cases} 0, & \mathbf{k} = \mathbf{0}, \\ \frac{4\pi}{|\mathbf{k}|^2} \exp\left(-\frac{|\mathbf{k}|^2}{4\alpha^2}\right), & \mathbf{k} \neq \mathbf{0}, \end{cases} \quad (11)$$

where α is the Ewald splitting parameter. Equation (11) is the Fourier transform of the smooth Ewald long-range kernel $\text{erf}(\alpha r)/r$. In a conventional Ewald decomposition this term is combined with a real-space pair contribution $\text{erfc}(\alpha r)/r$ so that their sum recovers the full Coulomb interaction. In the present neural potential, only the smooth mesh term is evaluated explicitly; the complementary short-range part is absorbed into the learned local energy. A smaller α gives a smoother mesh kernel but leaves more short-range electrostatics to the MPNN, whereas a larger α places more of the Coulomb interaction in the mesh channel and therefore requires a finer grid for comparable discretization accuracy. In practice, α is treated as a fixed hyperparameter.

The corrected electrostatic potential in reciprocal space is:

$$\tilde{\phi}(\mathbf{k}) = \tilde{G}(\mathbf{k}) \cdot \mathcal{C}(\mathbf{n}) \cdot \tilde{\rho}(\mathbf{k}), \quad (12)$$

and the real-space potential is recovered via inverse FFT:

$$\phi(\mathbf{r}_{n_x, n_y, n_z}) = \text{IFFT}[\tilde{\phi}]. \quad (13)$$

The reciprocal-space electrostatic energy is then implemented as

$$E^{\text{recip}} = \frac{1}{2V} \sum_{n_x, n_y, n_z} \rho_{\text{mesh}}(\mathbf{n}) \phi(\mathbf{n}), \quad (14)$$

where $V = |\det(\mathbf{C})|$ is the cell volume, and the $\mathbf{k} = \mathbf{0}$ term is excluded (as its contribution is canceled by the neutralizing background for charge-neutral systems).

2.3.5 Self-interaction correction

The reciprocal-space energy includes a spurious self-interaction of each Gaussian charge distribution with itself. For point charges, the self-energy correction is:

$$E_q^{\text{self}} = -\frac{\alpha}{\sqrt{\pi}} \sum_{i=1}^N q_i^2. \quad (15)$$

For point dipoles, the analogous Gaussian self-interaction yields [50]:

$$E_\mu^{\text{self}} = -\frac{2\alpha^3}{3\sqrt{\pi}} \sum_{i=1}^N |\boldsymbol{\mu}_i|^2. \quad (16)$$

Equations (15)–(16) are the continuum-limit expressions; they depend on the Ewald splitting parameter α and on the predicted charges or dipoles.

The total long-range electrostatic energy is:

$$E^{\text{lr}} = E^{\text{recip}} + E_q^{\text{self}} + E_\mu^{\text{self}}. \quad (17)$$

Every step in the PME pipeline—mesh assignment (with `index_put_` and `accumulate=True`), forward and inverse FFTs, Green’s function multiplication in k -space, and energy summation—is implemented using native differentiable PyTorch operations, enabling end-to-end gradient flow from the total energy to the network parameters $\boldsymbol{\theta}$ through the entire reciprocal-space solver [51].

2.4 Total energy and training

The total potential energy of the system is the sum of short-range and long-range contributions:

$$E_{\text{total}} = \underbrace{\sum_{i=1}^N E_i^{\text{sr}}}_{\text{short-range MPNN}} + \underbrace{E^{\text{lr}}(\{q_i\}, \{\boldsymbol{\mu}_i\}, \{\mathbf{r}_i\}, \mathbf{C})}_{\text{differentiable PME}}. \quad (18)$$

Atomic forces are obtained by analytical differentiation of the total energy:

$$\mathbf{F}_j = -\frac{\partial E_{\text{total}}}{\partial \mathbf{r}_j} = -\frac{\partial E^{\text{sr}}}{\partial \mathbf{r}_j} - \frac{\partial E^{\text{lr}}}{\partial \mathbf{r}_j}, \quad (19)$$

where both terms are computed via automatic differentiation. The long-range force term $\partial E^{\text{lr}}/\partial \mathbf{r}_j$ receives contributions through two channels: the explicit dependence of the mesh assignment on atomic positions, and the implicit dependence through the position-sensitive charge and dipole predictions $\partial q_i/\partial \mathbf{r}_j$ and $\partial \boldsymbol{\mu}_i/\partial \mathbf{r}_j$, which are captured by the computation graph.

The model is trained by minimizing a combined loss function:

$$\mathcal{L} = \lambda_E \cdot \frac{1}{N_{\text{batch}}} \sum_b \left(\frac{E_b^{\text{pred}} - E_b^{\text{ref}}}{N_b} \right)^2 + \lambda_F \cdot \frac{1}{3 \sum_b N_b} \sum_{b,i,\alpha} \left(F_{b,i,\alpha}^{\text{pred}} - F_{b,i,\alpha}^{\text{ref}} \right)^2, \quad (20)$$

where b indexes structures in the batch, N_b is the number of atoms in structure b , and λ_E , λ_F are user-defined weights. Optionally, virial stress can be included as an additional loss term for training on condensed-phase data.

Optimization uses the Adam or AdamW optimizer with grouped weight decay: embedding and readout layers receive no weight decay, interaction weights (tensor product coefficients) receive nonzero weight decay, and biases receive none. A linear learning rate warmup over the first N_{warmup} steps is followed by exponential decay or ReduceLROnPlateau scheduling.

3 Results

3.1 Example 1: charged dimer

We first examine the charged-dimer dataset as a controlled long-range molecular test case. Following the charged molecular dimer example discussed by King et al. [34], we use molecular-pair id 0 from the LODE/BioFragment molecular-dimer data [35]. The system is a neutral ion pair composed of a $\text{C}_3\text{N}_3\text{H}_{10}^+$ cation and a $\text{C}_2\text{O}_2\text{H}_3^-$ anion, giving 23 atoms per configuration. The monomer geometries are kept fixed and only the intermolecular separation is varied, so the dataset is essentially a charged binding curve rather than a thermally sampled molecular trajectory. The reference labels are HSE06 hybrid-DFT energies and forces with a many-body dispersion correction. The local split used here contains 10 training configurations with separations from 6.63 to 12.23 Å and 3 validation configurations from 13.09 to 15.00 Å. This example is useful because the electrostatic interaction is strong, the distinction between short-range and long-range descriptions is

easy to interpret, and the corresponding PME and Ewald calculations can be compared directly over a broad parameter range.

All charged-dimer models use the same five-layer HotPP with cutoff 5.0 Å, a polynomial cutoff with $p = 5$, and a Bessel-MLP radial layer with 8 basis functions and hidden widths [32, 32]. The long-range variants are named “charge-only” when only the charge head is enabled and “charge+dipole” when both the charge and dipole heads are enabled; each is run with either explicit Ewald summation or differentiable PME. The latent electrostatic variables are trained only from total energies and forces, without direct charge or dipole labels.

Figure 2 summarizes the first 1000 training epochs for the tested models. Three observations are most relevant. First, the long-range-augmented variants converge to substantially lower energy and force validation losses than the short-range-only baseline, showing that the charged-dimer interaction cannot be represented efficiently by a purely local model. Second, the force loss is especially sensitive to the long-range channel, consistent with the fact that forces probe the derivative of the electrostatic interaction and therefore accentuate deficiencies in a truncated local description. Third, the charge+dipole variants reach the lowest final-window validation losses overall, indicating that a dipolar response channel provides a meaningful correction beyond the leading monopolar term even in this relatively simple test case.

An important methodological question is whether the differentiable PME module reproduces the explicit Ewald reference with sufficient accuracy to be used as a drop-in replacement during training and inference. Figure 3 addresses this by comparing PME against the direct Ewald calculation on the same charged-dimer structures while varying the mesh spacing and interpolation order. As expected, the PME error decreases systematically when the grid is refined and when the assignment order is increased. The convergence is already smooth at moderate interpolation order, and order $p = 7$ gives the most stable low-error regime across the tested grid spacings.

The correction ablation in Fig. 3(c) is particularly important for the present implementation. Without the reciprocal-space deconvolution factor, the mesh assignment smooths the charge density too strongly, leaving a systematic bias in the reciprocal-space energy even when the grid is moderately fine. Including the correction markedly reduces this bias and restores the expected monotonic convergence toward the Ewald reference. In practice, this means that physically reliable PME behavior can be obtained on coarser meshes than would otherwise be required, which is exactly the regime where PME becomes attractive as a scalable substitute for explicit reciprocal-space summation.

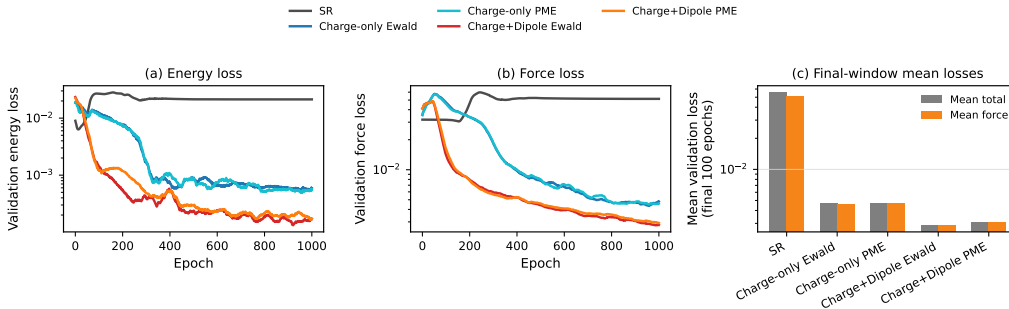


Figure 2: Charged-dimer training behavior over the first 1000 epochs. (a) Validation energy loss and (b) validation force loss for the short-range baseline and the long-range variants using either explicit Ewald summation or differentiable PME. Because the raw epoch-wise losses oscillate strongly before full convergence, panels (a) and (b) show 51-epoch centered moving averages in log-loss space to emphasize the optimization trend. Panel (c) compares the mean total and force validation losses over the final 100 epochs, computed from the original epoch-wise values. The key trend is that long-range augmentation consistently improves optimization, and that the charge+dipole models attain the lowest final-window losses.

Quantitatively, for assignment order $p = 7$ with the correction enabled, the mean PME–Ewald energy difference per atom is 3.47×10^{-9} eV at grid spacing 0.70 \AA and 1.83×10^{-9} eV at 0.28 \AA ; the corresponding force RMSE decreases from 2.86×10^{-7} to 9.91×10^{-9} eV/ \AA . Disabling the correction at 0.28 \AA raises the energy difference per atom to 3.18×10^{-3} eV and the force RMSE to 1.70×10^{-3} eV/ \AA , demonstrating that the deconvolution correction is essential for the reported mesh accuracy.

Taken together, the charged-dimer results establish two points that motivate the rest of the paper. On the modeling side, they show that adding explicit learned electrostatics improves both optimization and final validation behavior relative to a purely local baseline, with the charge+dipole formulation being the most effective variant among those tested. On the numerical side, they show that the differentiable PME solver can reproduce direct Ewald energies and forces to controlled accuracy, provided that a sufficiently smooth assignment order and the reciprocal-space influence correction are used.

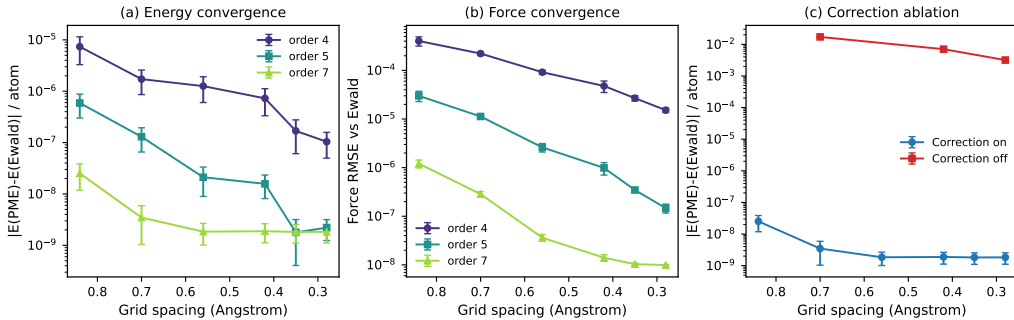


Figure 3: PME–Ewald comparison on the charged-dimer test set. (a) energy difference per atom and (b) force RMSE between PME and explicit Ewald as a function of mesh spacing for several assignment orders. (c) Ablation of the reciprocal-space influence correction at fixed order $p = 7$. The corrected PME converges systematically toward the Ewald reference, while omitting the correction produces noticeably larger residual energy errors at the same mesh resolution.

3.2 Example 2: molten NaCl

The molten-NaCl example tests whether the same long-range construction remains useful in a dense ionic environment and whether the reciprocal solver retains its expected scaling advantage beyond the small charged-dimer system. The structures are derived from the liquid-NaCl dataset of Faller et al. [36], which contains 1014 configurations with 64 Na and 64 Cl atoms. In our converted split, 90% configurations are used for training and 10% for validation.

The molten-NaCl models use a HotPP backbone with longrange method PME: cutoff 6.0 \AA , five interaction layers, $n_{\text{embedding}} = n_{\text{hidden}} = 64$, a polynomial cutoff with $p = 5$, and a Bessel-MLP radial layer with 8 basis functions and hidden widths [64, 64]. As above, the latent charges and dipoles are not directly supervised. The replicated NaCl supercells used in the timing study are generated only from the validation structures and are not used as independent machine-learning generalization data.

We first examine the optimization behavior before comparing final RMSE values. Both long-range variants reduce the validation total loss and force loss relative to the short-range model, with the charge+dipole model giving the lowest losses over the late training window. The final validation RMSE values are summarized in Table 1, and the force trend is shown graphically in Fig. 4(a). The clearest accuracy trend is in the forces: the force RMSE decreases from 8.46 meV/\AA for the short-range baseline to 6.76 meV/\AA with charge-only PME and to 5.92 meV/\AA with the charge+dipole PME model.

Thus, the explicit long-range channel reduces the force error by approximately 30% relative to the local baseline.

Table 1: Molten-NaCl validation RMSE for the short-range baseline and the PME-augmented long-range models. Energy errors are reported per atom.

Model	Energy (meV/atom)	Force (meV/Å)
Short-range	0.573	8.46
Charge-only PME	0.763	6.76
Charge+dipole PME	0.845	5.92

The energy RMSE is slightly larger for the two long-range variants, increasing from 0.573 meV/atom to 0.763 and 0.845 meV/atom. These differences are below 0.3 meV/atom in absolute terms, and all three values remain in the sub-meV/atom regime. We therefore regard the energy differences as effectively at the numerical-error level for the present comparison, rather than as evidence for a meaningful degradation of the potential. The force RMSE provides the more diagnostic metric here, and it consistently improves when the explicit long-range channel is included, as highlighted in Fig. 4(a).

To isolate the numerical cost of the long-range solver, we also evaluated molten-NaCl supercells from 128 to 16,000 atoms. These replicated structures are used only as timing and numerical-consistency tests; they are not independent machine-learning generalization data. For the supercells where explicit Ewald was run, PME and Ewald agree to approximately $1.7\text{--}1.8 \times 10^{-9}$ eV/atom in energy, with force-norm differences below 1.3×10^{-10} per atom. The timing comparison in Fig. 4(b) shows the expected crossover: explicit Ewald is faster at 128 atoms because the FFT overhead dominates, while PME becomes faster at 512 atoms. The corresponding Ewald/PME speedup in Fig. 4(c) reaches 4.82 at 1024 atoms and 10.36 at 1536 atoms. For larger cells, explicit Ewald was not run because of its memory and time cost, while PME remains practical up to the 16,000-atom cell with a median frame time of 16.84 ms and an average peak memory footprint of 1.17 GB, as shown in Fig. 4(d).

These force-accuracy and scaling trends are collected in Fig. 4, which keeps the RMSE comparison together with the reciprocal-solver timing and memory data.

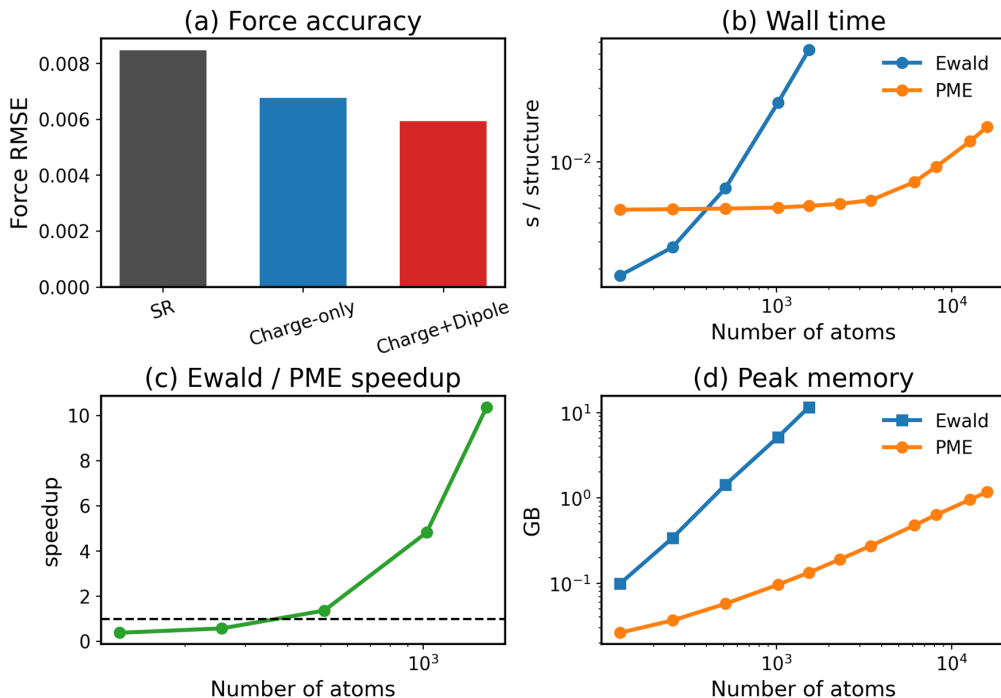


Figure 4: Molten-NaCl accuracy and reciprocal-solver scaling summary. (a) Force RMSE for the short-range, charge-only PME, and charge+dipole PME models. (b) Median per-frame wall time for explicit Ewald and differentiable PME on replicated molten-NaCl supercells. (c) Ewald/PME speedup on the cells where explicit Ewald was run. (d) PME peak memory use, including the 16,000-atom cell where explicit Ewald is intentionally omitted.

4 Discussion

We have introduced a differentiable particle-mesh Ewald framework for learning long-range electrostatics within an $E(n)$ -equivariant Cartesian tensor message passing potential. The model predicts atomic charges and dipoles from local equivariant features, evaluates their long-range interaction through a fully differentiable FFT-based solver, and combines this energy with the short-range site energy predicted by HotPP. This construction keeps the favorable locality and equivariance properties of modern MLIPs while restoring the non-local electrostatic coupling required for ionic, polar, and interfacial systems.

The most important conceptual point is that the present work is not positioned as a replacement for recent multipole-based Ewald MLIPs, but as a scalable realization of the same emerging paradigm. Kim et al. [33]

have shown that locally predicted multipoles can recover substantial long-range physics from energy and force supervision alone. Our contribution is to make this strategy compatible with the particle-mesh algorithms used in production MD, including differentiable FFTs, spline assignment, and mesh correction. In this sense, the method addresses a practical bottleneck rather than disputing the physical premise of learned multipoles.

Several limitations should be acknowledged. The two example studies reported here focus on monopoles and dipoles; quadrupolar channels are a natural next extension of the Cartesian tensor representation but are not used in the charged-dimer and molten-NaCl results above. The polarization response is non-self-consistent: charges and dipoles are predicted in one forward pass from local features, rather than iteratively relaxed in the field generated by all other atoms. This choice keeps the model efficient and stable, but it may miss feedback effects that are important in strongly polarizable materials. Finally, as with all supervised MLIPs, transferability is bounded by the thermodynamic states and chemical environments represented in the training data.

The combination of FFT-accelerated long-range electrostatics and end-to-end differentiability opens a practical route to scalable simulations of polar liquids, ionic solids, perovskites, solvated interfaces, and defect-containing materials with learned long-range interactions. Future extensions will include quadrupolar PME channels, explicit field-dependent response, and tighter integration with active-learning workflows for generating long-range-sensitive training data.

5 Conclusions

We presented a differentiable particle-mesh long-range electrostatic formulation for equivariant neural network potentials with learned atomic charges and dipoles. By replacing explicit reciprocal-space Ewald summation with an FFT-based particle-mesh solver, the framework targets $O(N \log N)$ evaluation of the smooth long-range channel while preserving end-to-end gradient flow through the electrostatic energy, forces, and latent multipole predictions. The Cartesian tensor representation of HotPP provides a natural interface to this long-range module: scalar features predict charges, vector features predict dipoles, and the short-range site energy absorbs the local complementary part of the interaction.

The charged-dimer test case shows that learned long-range channels improve optimization and that corrected PME can reproduce explicit Ewald energies and forces on the same structures. The molten-NaCl example shows

force-error reduction from charge and dipole channels in a condensed ionic system and a clear timing crossover where PME becomes substantially faster than explicit Ewald summation. Together, these results support the central claim that differentiable particle-mesh electrostatics can provide Ewald-level long-range accuracy at particle-mesh cost within an equivariant neural-network potential.

Code availability

The source code for the HotPP-LR implementation and the example workflows used in this work is available in the `1r` branch of the HotPP GitLab repository: <https://gitlab.com/bigd4/hotpp>.

References

- [1] J. Behler and M. Parrinello, “Generalized neural-network representation of high-dimensional potential-energy surfaces,” *Phys. Rev. Lett.* **98**, 146401 (2007).
- [2] A. P. Bartók, M. C. Payne, R. Kondor, and G. Csányi, “Gaussian approximation potentials: The accuracy of quantum mechanics, without the electrons,” *Phys. Rev. Lett.* **104**, 136403 (2010).
- [3] A. P. Thompson, L. P. Swiler, C. R. Trott, S. M. Foiles, and G. J. Tucker, “Spectral neighbor analysis method for automated generation of quantum-accurate interatomic potentials,” *J. Comput. Phys.* **285**, 316–330 (2015).
- [4] A. V. Shapeev, “Moment tensor potentials: A class of systematically improvable interatomic potentials,” *Multiscale Model. Simul.* **14**, 1153–1173 (2016).
- [5] J. S. Smith, O. Isayev, and A. E. Roitberg, “ANI-1: An extensible neural network potential with DFT accuracy at force field computational cost,” *Chem. Sci.* **8**, 3192–3203 (2017).
- [6] L. Zhang, J. Han, H. Wang, R. Car, and W. E, “Deep Potential Molecular Dynamics: A scalable model with the accuracy of quantum mechanics,” *Phys. Rev. Lett.* **120**, 143001 (2018).

- [7] K. T. Schütt, H. E. Sauceda, P.-J. Kindermans, A. Tkatchenko, and K.-R. Müller, “SchNet – a deep learning architecture for molecules and materials,” *J. Chem. Phys.* **148**, 241722 (2018).
- [8] K. T. Schütt, O. T. Unke, and M. Gastegger, “Equivariant message passing for the prediction of tensorial properties and molecular spectra,” *Proc. Mach. Learn. Res.* **139**, 9377–9388 (2021).
- [9] S. Batzner, A. Musaelian, L. Sun, M. Geiger, J. P. Mailoa, M. Kornbluth, N. Molinari, T. E. Smidt, and B. Kozinsky, “E(3)-equivariant graph neural networks for data-efficient and accurate interatomic potentials,” *Nat. Commun.* **13**, 2453 (2022).
- [10] I. Batatia, D. P. Kovács, G. N. C. Simm, C. Ortner, and G. Csányi, “MACE: Higher Order Equivariant Message Passing Neural Networks for Fast and Accurate Force Fields,” *Adv. Neural Inf. Process. Syst.* **35**, 11423–11436 (2022).
- [11] A. Musaelian, S. Batzner, A. Johansson, L. Sun, C. J. Owen, M. Kornbluth, and B. Kozinsky, “Learning local equivariant representations for large-scale atomistic dynamics,” *Nat. Commun.* **14**, 579 (2023).
- [12] J. Wang, Y. Wang, H. Zhang, Z. Yang, Z. Liang, J. Shi, H.-T. Wang, D. Xing, and J. Sun, “E(n)-equivariant Cartesian tensor message passing interatomic potential,” *Nat. Commun.* **15**, 7607 (2024).
- [13] O. T. Unke, S. Chmiela, H. E. Sauceda, M. Gastegger, I. Poltavsky, K. T. Schütt, A. Tkatchenko, and K.-R. Müller, “Machine learning force fields,” *Chem. Rev.* **121**, 10142–10186 (2021).
- [14] Y. You, D. Zhang, F. Wu, X. Cao, Y. Sun, Z.-Z. Zhu, and S. Wu, “Principal component analysis enables the design of deep learning potential precisely capturing LLZO phase transitions,” *npj Comput. Mater.* **10**, 57 (2024).
- [15] E. Prodan and W. Kohn, “Nearsightedness of electronic matter,” *Proc. Natl. Acad. Sci. USA* **102**, 11635–11638 (2005).
- [16] D. M. Anstine and O. Isayev, “Machine learning interatomic potentials and long-range physics,” *J. Phys. Chem. A* **127**, 2417–2431 (2023).
- [17] W. J. Mortier, S. K. Ghosh, and S. Shankar, “Electronegativity-equalization method for the calculation of atomic charges in molecules,” *J. Am. Chem. Soc.* **108**, 4315–4320 (1986).

- [18] A. K. Rappé and W. A. Goddard III, “Charge equilibration for molecular dynamics simulations,” *J. Phys. Chem.* **95**, 3358–3363 (1991).
- [19] F. H. Streitz and J. W. Mintmire, “Electrostatic potentials for metal-oxide surfaces and interfaces,” *Phys. Rev. B* **50**, 11996–12003 (1994).
- [20] J. Behler, “Constructing high-dimensional neural network potentials: A tutorial review,” *Int. J. Quantum Chem.* **115**, 1032–1050 (2015).
- [21] T. W. Ko, J. A. Finkler, S. Goedecker, and J. Behler, “A fourth-generation high-dimensional neural network potential with accurate electrostatics including non-local charge transfer,” *Nat. Commun.* **12**, 398 (2021).
- [22] B. T. Thole, “Molecular polarizabilities calculated with a modified dipole interaction,” *Chem. Phys.* **59**, 341–350 (1981).
- [23] P. Ren and J. W. Ponder, “Polarizable atomic multipole water model for molecular mechanics simulation,” *J. Phys. Chem. B* **107**, 5933–5947 (2003).
- [24] O. T. Unke and M. Meuwly, “PhysNet: A neural network for predicting energies, forces, dipole moments, and partial charges,” *J. Chem. Theory Comput.* **15**, 3678–3693 (2019).
- [25] O. T. Unke, S. Chmiela, M. Gastegger, K. T. Schütt, H. E. Sauceda, and K.-R. Müller, “SpookyNet: Learning force fields with electronic degrees of freedom and nonlocal effects,” *Nat. Commun.* **12**, 7273 (2021).
- [26] L. Zhang, H. Wang, M. C. Muniz, A. Z. Panagiotopoulos, R. Car, and W. E, “A deep potential model with long-range electrostatic interactions,” *J. Chem. Phys.* **156**, 124107 (2022).
- [27] R. Guo, H. Yu, L. Hong, S. Chen, X. Gong, and H. Xiang, “Capturing long-range interactions with a reciprocal-space neural network,” *Phys. Rev. B* **113**, 174101 (2026).
- [28] A. Grisafi and M. Ceriotti, “Incorporating long-range physics in atomic-scale machine learning,” *J. Chem. Phys.* **151**, 204105 (2019).
- [29] K. K. Huguenin-Dumittan, P. Loche, N. Haoran, and M. Ceriotti, “Physics-inspired equivariant descriptors of nonbonded interactions,” *J. Phys. Chem. Lett.* **14**, 9612–9618 (2023).

- [30] A. Kosmala, J. Gasteiger, N. Gao, and S. Günnemann, “Ewald-based long-range message passing for molecular graphs,” *Proc. Mach. Learn. Res.* **202**, 17544–17563 (2023).
- [31] E. Rumiantsev, M. F. Langer, T.-E. Sodjargal, M. Ceriotti, and P. Loche, “Learning long-range representations with equivariant messages,” Preprint at arXiv, arXiv:2507.19382 (2026).
- [32] B. Cheng, “Latent Ewald summation for machine learning of long-range interactions,” *npj Comput. Mater.* **11**, 80 (2025).
- [33] D. Kim, D. S. King, Y. Park, R. Savoj, S. Hamel, X. Wang, and B. Cheng, “Polarizable atomic multipoles for learning long-range electrostatics,” Preprint at arXiv, arXiv:2605.05746 (2026).
- [34] D. S. King, D. Kim, P. Zhong, and B. Cheng, “Machine learning of charges and long-range interactions from energies and forces,” *Nat. Commun.* **16**, 8763 (2025).
- [35] L. A. Burns, J. C. Faver, Z. Zheng, M. S. Marshall, D. G. A. Smith, K. Vanommeslaeghe, A. D. MacKerell, K. M. Merz, and C. D. Sherill, “The BioFragment Database (BFDdb): An open-data platform for computational chemistry analysis of noncovalent interactions,” *J. Chem. Phys.* **147**, 161727 (2017).
- [36] C. Faller, M. Kaltak, and G. Kresse, “Density-based long-range electrostatic descriptors for machine learning force fields,” *J. Chem. Phys.* **161**, 214701 (2024).
- [37] P. P. Ewald, “Die Berechnung optischer und elektrostatischer Gitterpotentiale,” *Ann. Phys.* **369**, 253–287 (1921).
- [38] J. Kolafa and J. W. Perram, “Cutoff errors in the Ewald summation formulae for point charge systems,” *Mol. Simul.* **9**, 351–368 (1992).
- [39] D. A. Case, T. E. Cheatham III, T. Darden, H. Gohlke, R. Luo, K. M. Merz Jr., A. Onufriev, C. Simmerling, B. Wang, and R. J. Woods, “The Amber biomolecular simulation programs,” *J. Comput. Chem.* **26**, 1668–1688 (2005).
- [40] B. R. Brooks, C. L. Brooks III, A. D. Mackerell Jr., L. Nilsson, R. J. Petrella, B. Roux, Y. Won, G. Archontis, C. Bartels, S. Boresch, A. Caffisch, L. Caves, Q. Cui, A. R. Dinner, M. Feig, S. Fischer, J. Gao, M. Hodoscek, W. Im, K. Kuczera, T. Lazaridis, J. Ma, V. Ovchinnikov,

- E. Paci, R. W. Pastor, C. B. Post, J. Z. Pu, M. Schaefer, B. Tidor, R. M. Venable, H. L. Woodcock, X. Wu, W. Yang, D. M. York, and M. Karplus, "CHARMM: The biomolecular simulation program," *J. Comput. Chem.* **30**, 1545–1614 (2009).
- [41] M. J. Abraham, T. Murtola, R. Schulz, S. Páll, J. C. Smith, B. Hess, and E. Lindahl, "GROMACS: High performance molecular simulations through multi-level parallelism from laptops to supercomputers," *SoftwareX* **1–2**, 19–25 (2015).
- [42] J. C. Phillips, D. J. Hardy, J. D. C. Maia, J. E. Stone, J. V. Ribeiro, R. C. Bernardi, R. Buch, G. Fiorin, J. Hénin, W. Jiang, R. McGreevy, M. C. R. Melo, B. K. Radzak, R. D. Skeel, A. Singharoy, Y. Wang, B. Roux, A. Aksimentiev, Z. Luthey-Schulten, L. V. Kalé, K. Schulten, C. Chipot, and E. Tajkhorshid, "Scalable molecular dynamics on CPU and GPU architectures with NAMD," *J. Chem. Phys.* **153**, 044130 (2020).
- [43] A. P. Thompson, H. M. Aktulga, R. Berger, D. S. Bolintineanu, W. M. Brown, P. S. Crozier, P. J. in 't Veld, A. Kohlmeyer, S. G. Moore, T. D. Nguyen, R. Shan, M. J. Stevens, J. Tranchida, C. Trott, and S. J. Plimpton, "LAMMPS – a flexible simulation tool for particle-based materials modeling at the atomic, meso, and continuum scales," *Comput. Phys. Commun.* **271**, 108171 (2022).
- [44] T. Darden, D. York, and L. Pedersen, "Particle mesh Ewald: An $N \cdot \log(N)$ method for Ewald sums in large systems," *J. Chem. Phys.* **98**, 10089–10092 (1993).
- [45] U. Essmann, L. Perera, M. L. Berkowitz, T. Darden, H. Lee, and L. G. Pedersen, "A smooth particle mesh Ewald method," *J. Chem. Phys.* **103**, 8577–8593 (1995).
- [46] P. Loche, K. K. Huguenin-Dumittan, M. Honarmand, Q. Xu, E. Rumiantssev, W. B. How, M. F. Langer, and M. Ceriotti, "Fast and flexible long-range models for atomistic machine learning," *J. Chem. Phys.* **162**, 142501 (2025).
- [47] M. Deserno and C. Holm, "How to mesh up Ewald sums. I. A theoretical and numerical comparison of various particle mesh routines," *J. Chem. Phys.* **109**, 7678–7693 (1998).

- [48] M. Deserno and C. Holm, “How to mesh up Ewald sums. II. An accurate error estimate for the particle–particle–particle-mesh algorithm,” *J. Chem. Phys.* **109**, 7694–7701 (1998).
- [49] R. W. Hockney and J. W. Eastwood, *Computer Simulation Using Particles* (IOP Publishing Ltd, 1988).
- [50] A. Toukmaji, C. Sagui, J. Board, and T. Darden, “Efficient particle-mesh Ewald based approach to fixed and induced dipolar interactions,” *J. Chem. Phys.* **113**, 10913–10927 (2000).
- [51] A. Paszke, S. Gross, F. Massa, A. Lerer, J. Bradbury, G. Chanan, T. Killeen, Z. Lin, N. Gimelshein, L. Antiga, A. Desmaison, A. Köpf, E. Yang, Z. DeVito, M. Raison, A. Tejani, S. Chilamkurthy, B. Steiner, L. Fang, J. Bai, and S. Chintala, “PyTorch: An imperative style, high-performance deep learning library,” *Adv. Neural Inf. Process. Syst.* **32**, 8024–8035 (2019).